Surface Topography:
Metrology and
Properties

PURPOSE-LED
PUBLISHING™

PAPER • OPEN ACCESS

Correlating topographic features and mechanisms for macropitting, micropitting, and electrical pitting in bearing steel contacts

To cite this article: Zaihao Tian *et al* 2026 *Surf. Topogr.: Metrol. Prop.* **14** 025005

IOP Publishing Surf. Topogr.: Metrol. Prop. 14 (2026) 025005 https://doi.org/10.1088/2051-672X/ae5f36

Surface Topography: Metrology and Properties

RECEIVED
18 January 2026

REVISED
19 February 2026

ACCEPTED FOR PUBLICATION
14 April 2026

PUBLISHED
23 April 2026

PAPER

Correlating topographic features and mechanisms for macropitting, micropitting, and electrical pitting in bearing steel contacts

Zaihao Tian[1,*], **Terence Harvey**[1], **Shifeng Zhuo**[2], **Haidong Pan**[2] **and Robert Wood**[1]

[1] National Centre for Advanced Tribology, University of Southampton, Southampton SO17 1BJ, United Kingdom
[2] Department of Mechanical Engineering, University of Southampton, Southampton SO17 1BJ, United Kingdom
[*] Author to whom any correspondence should be addressed.

E-mail: Zaihao.Tian@soton.ac.uk

Keywords: macropitting, micropitting, electrical pitting, rolling–sliding contact, surface topography

Abstract

Pitting is a critical damage mode in rolling–sliding contacts that can arise from distinct mechanisms, including rolling contact fatigue and electrically induced discharge. This paper presents insights into the formation and characteristics of macropitting, micropitting, and electrical pitting in rolling–sliding contacts of bearing steels. Experiments were conducted using a TE74 twin-disc tribometer under controlled lubrication and electrical conditions. Under boundary to mixed lubrication, macropitting and micropitting were generated using a base oil and a zinc dithiophosphate-enriched oil, respectively. Electrical pitting was produced by applying a low electrical potential across the lubricated contact under elastohydrodynamic lubrication conditions. The three pitting modes exhibited distinct pit morphologies, crack features, and surface topography evolution. Macropitting was characterised by large, irregular pits formed through aggressive secondary crack propagation, whereas micropitting produced smaller, crescent-shaped pits with limited crack growth. Electrical pitting resulted in near-circular pits without surrounding cracks, indicating a discharge-dominated damage mechanism. Roughness parameters also revealed mechanism-dependent surface modifications, providing a unified topography-based framework for differentiating fatigue-driven and electrically induced pitting.

1. Introduction

Pitting is recognised as a critical tribological problem in rolling and sliding contacts, as it can drastically shorten component life and compromise machine reliability [1, 2]. As bearings and gears are increasingly required to transmit higher loads, meet stricter efficiency targets, and in some applications operate under electrical potentials, their susceptibility to pitting damage has become more pronounced [1, 3, 4]. This challenge is particularly evident in applications such as wind turbine drivetrains [5, 6], electric motors and generators [7, 8], aircraft engines [9] and rail-axle bearings [10], where downtime and failure costs are substantial.

Based on their mechanisms and characteristic geometry, three primary forms of pitting, macropitting, micropitting, and electrical pitting, are commonly identified in rolling–sliding contacts. Macropitting and micropitting are failure modes associated with rolling contact fatigue (RCF). Macropitting consists of fully developed craters with lateral dimensions of hundreds of micrometres and depths of tens to hundreds of micrometres, originating from surface or subsurface fatigue cracks under repeated contact stresses [11]. Micropitting appears as surface-initiated shallow pits, typically with depths of up to 20 μm, and is primarily caused by plastic deformation at the asperity level under cyclic contact stresses [12, 13]. In contrast, electrical pitting occurs when an electrical potential across the lubricating film, such as that caused by common-mode voltages from inverter-driven motors [8], exceeds the dielectric strength of the lubricant, resulting in localised electrical breakdowns. The transient currents can cause local melting and micro-cratering of the raceway and roller surface of a bearing, leading to electrical pits [8, 14, 15].

To identify pitting mechanisms and evaluate damage severity, a variety of experimental characterisation techniques and surface descriptors have been employed. Topographic parameters quantifying surface height and distribution are widely used to differentiate among pitting mechanisms and to assess the extent. Among various studies, roughness amplitude and functional parameters, such as root-mean-square (RMS) deviation (R_q for profile or S_q for 3D areal form), maximum height of peaks (R_p/S_p), maximum depth of valleys (R_v/S_v), skewness (R_{sk}/S_{sk}), kurtosis (R_{ku}/S_{ku}), core roughness depth (R_k/S_k), reduced peak height (R_{pk}/S_{pk}), and reduced valley depth (R_{vk}/S_{vk}), have been identified as key indicators of pitting mode and severity.

The RMS deviation represents the standard deviation of the surface height distribution [16]. The maximum valley depth corresponds to the vertical distance between the deepest valley and the mean line of the surface profile, while the maximum peak height represents the vertical distance between the highest peak and the mean line. The skewness describes the asymmetry of the height distribution about the mean line, with skewness = 0 indicating a symmetrical distribution. Negative skewness is associated with peak removal or deep valleys, whereas positive skewness indicates surfaces dominated by high peaks [16]. The kurtosis characterises the sharpness of the height distribution, with kurtosis <3 indicating relatively smooth surfaces and kurtosis >3 reflecting the presence of pronounced peaks and deep valleys [16].

These amplitude parameters have been widely used to characterise changes in surface topography [17] or surface damage such as pitting [18–20], spalling, and scuffing [21]. Harvey *et al* studied changes in surface topography of bearing steel discs after running-in using R_q, R_p, and R_v and found reduction in these parameters due to surface smoothing. In contrast, pitting damage has been shown to increase RMS deviation and kurtosis while making skewness more negative. Roy *et al* [18] examined changes in R_q, R_{sk}, and R_{ku} during micropitting tests and found that R_q increased with micropitting propagation, accompanied by decreasing R_{sk} and increasing R_{ku}. Prajapati and Tiwari [19, 20] investigated the evolution of micropitting and associated surface roughness parameters under varying slide-to-roll ratios (SRRs). Similarly, S_q was found to increase with micropitting severity as SRR rose from 5% to 10% [19]. It was further reported that as pitting progressed, S_v increased with decreasing S_{sk} and increasing S_{ku}, indicating formation of valleys and removal of surface peaks [20]. Poletto *et al* [21] characterised micropitting, macropitting, spalling and scuffing on gears using S_q and S_{sk}. Negative S_{sk} was corresponded to the presence of micropitting, macropitting and spalling, and S_q exhibited a clear correlation with increasing damage severity.

Furthermore, R_k, R_{pk} and R_{vk} have been shown to be sensitive to micropitting [22] and pitting [23] in gears, where experimental investigations have shown that the occurrence of pitting was typically accompanied by an increase in R_k, R_{vk} and a decrease in R_{pk} [22, 23], reflecting the formation of deep valleys and the removal of surface peaks.

Fatigue-related pitting and electrical pitting are often studied separately. To date, they have not been compared within a unified experimental and metrology framework, in which surface topography features are analysed using consistent measurement methods and parameters. The present work addresses this gap by producing macropitting, micropitting, and electrical pitting using a controlled twin-disc tribometer setup. The bearing steel is kept constant throughout, while the initial surface roughness and lubricant formulation are varied to promote different pitting mechanisms. Pitting morphology is characterised using optical 3D profilometer and SEM, while surface topography is quantified through 2D surface roughness measurements. The operating conditions leading to different pitting mechanisms are further compared and identified, offering insights for predicting and mitigating specific pitting modes in practical applications.

2. Methodology

2.1. Experimental equipment and materials

In order to reproduce bearing pitting under controlled laboratory conditions, rolling–sliding experiments were conducted using a TE74 twin-disc configuration (Phoenix Tribology Ltd, Kingsclere, UK). Figure 1 depicts the test configuration, in which a pair of discs operates under lubricated rolling or rolling–sliding contact conditions. The normal load is applied to the disc interface via a bellows-driven pneumatic actuator acting through a pivot-mounted load arm.

In each test, a pair of discs made of AISI52100 bearing steel (Schaeffler Technologies GmbH & Co. KG, Schweinfurt, Germany) was used. The material and disc geometries simulated the roller-raceway contact in rolling element bearings. The chemical composition and mechanical properties of the bearing steel have been reported in [24]. As illustrated in figure 1, Disc1 had a diameter of 39 mm with a cylindrical surface geometry, while Disc 2 had a diameter of 41 mm with a crowned surface geometry with a transverse diameter of 100 mm. This combination resulted in a self-aligning elliptical contact, which effectively minimises stresses induced by edges.

Disc 1 had a roughness R_q of 0.03 μm, while Disc 2 had an R_q of 0.04 μm or 0.026 μm for different lubrication conditions. An R_q of 0.03–0.04 μm is typical for rolling element bearings [25]. Disc 2 was roughened to R_q = 0.26 μm in selected tests

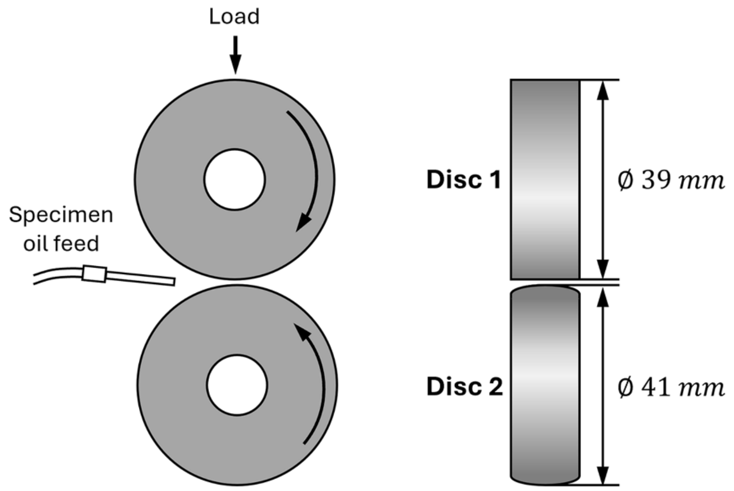

Figure 1. TE74 twin-disc setup.

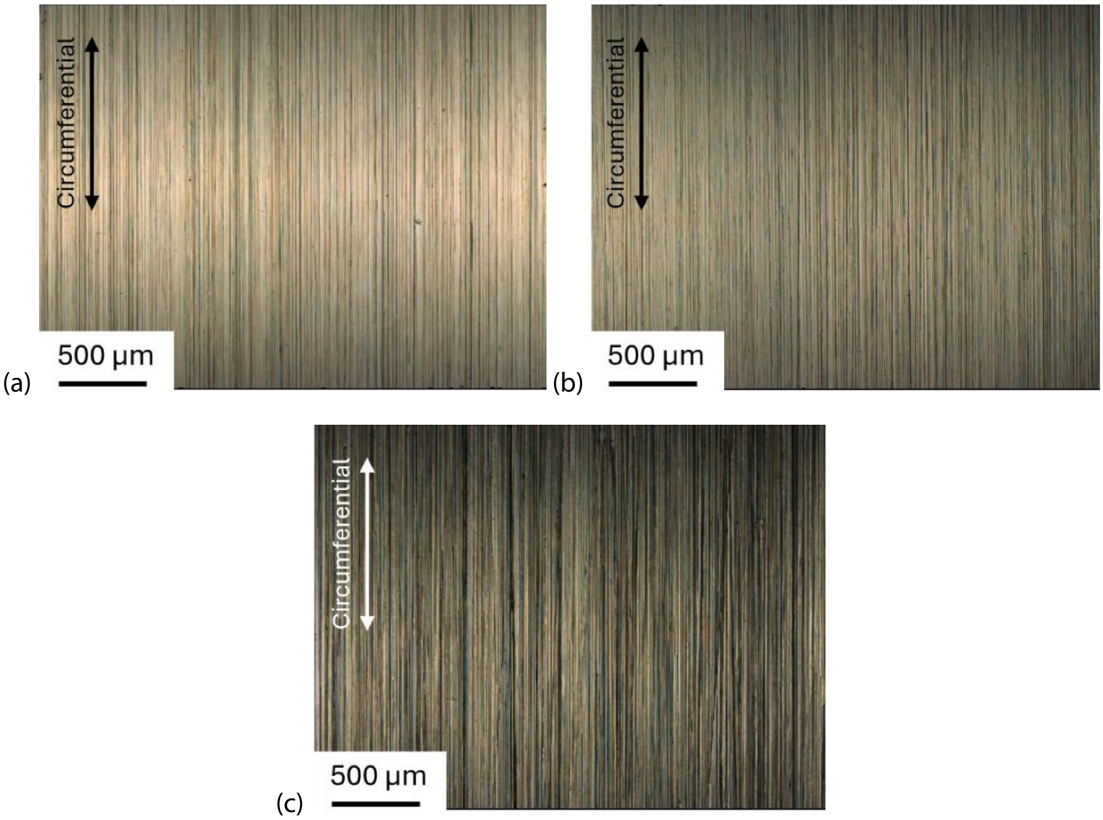

Figure 2. Optical images of untested (a) Disc 1 with R_q of 0.03 μm, (b) Disc 2 with R_q of 0.04 μm, and (c) Disc 2 with R_q of 0.26 μm.

to accelerate pitting formation. Optical images of untested Disc1 and Disc 2 surfaces are shown in figure 2.

Two lubricants were used in this study. The first was SpectraSyn 8 Polyaphaolefin (PAO) base oil, provided by Exxon Mobil Corporation, Texas, US, with properties provided in table 1. PAO oils are synthetic and commonly used in RCF studies [26, 27], as their well-characterised and stable properties provide a reproducible baseline for isolating the effects of surface conditions, operating conditions, and additive packages.

The second lubricant was the PAO8 base oil mixed with 2 wt% HiTEC 1656, which is a primary-secondary mixed zinc dithiophosphate (ZDDP) additive, provided by AFTON Chemical Corporation, Bracknell. Details of this additive are provided in table 2. The addition of 2 wt% ZDDP is expected to cause only a marginal increase in viscosity, so the viscosity of the ZDDP-enriched oil can be considered

Table 1. Properties of PAO8 oil.

Properties	Metric
Kinematic viscosity, cSt, 100 °C	8.0
Kinematic viscosity, cSt, 40 °C	48
Viscosity index	139
Flash point, °C	>286
Specific gravity (60/60 °F)	0.833
Dielectric strength	37.7 kV (ASTM D877)

Table 2. Compositions of ZDDP additive.

Alcohol used	Zinc	% Phosphorus	% Sulphur
IPA, IBA, 2-EH	8.35	9.2	17.8

comparable to that of the base PAO8 oil for the purposes of lubrication condition estimation. As reported in previous studies [28, 29], adding ZDDP into PAO base oils can increase the dielectric strength by approximately 11%–29%. This is attributed to the polar functional groups in ZDDP, which can trap charge carriers and reduce their mobility [29].

2.2. Test conditions and execution

The test conditions are summarised in table 3. These conditions were selected based on studies reported in the literature [26, 27, 30–33] in which pitting was generated. In these studies, the maximum Hertzian contact pressure was typically controlled between 1.5 and 3.14 GPa. Lubrication conditions were controlled to produce boundary to mixed lubrication regimes, to promote sufficient asperity interactions. SRRs between 1 and 30% were applied to introduce controlled sliding to promote crack and pitting initiation.

In this study, all the tests were carried out under a load of 2.42 kN, which produced a maximum Hertzian contact pressure of 2.5 GPa, representative of typical rolling element bearing contacts [34, 35]. The oil temperature was maintained at 100 ± 5 °C to promote boundary to mixed lubrication conditions through reduced lubricant viscosity and to activate the ZDDP additive.

The tests were categorised into three types: ‘Macropitting’ (M-series), ‘Micropitting’ (MP-series), and ‘Electrical pitting’ (E-series). The macropitting tests were conducted with PAO8 base oil. As a baseline test, test M1 used a smooth–smooth disc pair (R_q 0.03 μm vs 0.04 μm), and no pitting was anticipated. In M2 and M3, Disc 2 was rougher to promote and localise pitting on Disc 1, reducing the lambda ratio (λ) to 0.23. The ‘Micropitting’ tests were identical except the lubricant was changed to the ZDDP enriched oil. In the ‘Electrical pitting’ group, a smooth–smooth surface combination was used to achieve higher lambda ratios, increasing the separation between opposing asperities and providing conditions suitable for dielectric breakdown and electrical pitting. E1 replicated the conditions of MP1 except that an external potential was applied across the discs. In addition, E2 and E3 employed different rotational speeds and SRR values to validate the repeatability of electrical pitting generation.

Macropitting and micropitting are fatigue pitting modes and therefore require extended durations for crack initiation and propagation. In contrast, electrical pitting is caused by lubricant dielectric breakdown rather than fatigue accumulation. Therefore, damage can develop within a much shorter duration and 0.5–1.5 million cycles is sufficient to generate representative electrical pitting. Macropitting and micropitting tests were repeated under comparable conditions, and pitting was consistently reproduced [36]. Electrical pitting tests were repeated twice with pitting observed in the repeats.

2.2.1. *Electric test configuration*

An external electrical circuit powered by a 10 V power supply was used to apply voltage across the two rotating discs, as schematically shown in figure 3. The voltage was chosen based on literature evidence. Shaft voltage peaks of up to 8 V have been reported in inverter-driven motors [37], representative of practical conditions. In addition, previous experimental studies employing a similar test configuration used a 15 V power supply and successfully generated electrical pitting [33]. The rig’s contact potential different setup of brushes and slip rings was used to connect the circuit. A 30 kΩ current-limiting resistor was employed to restrict the discharge current to approximately 0.33 mA, ensuring that breakdown events manifest as localised electrical discharge machining (EDM)-like micro-discharges rather than catastrophic melting or sustained arcing. A Picoscope 4424 oscilloscope (Pico Technology, Eaton Socon, UK) was used to measure the voltage between the discs.

In the ‘Electrical pitting’ tests, the minimum oil film thickness was calculated using the Hamrock–Dowson EHL film-thickness model [38] to be approximately 58–96 nm. Using the bulk

Table 3. Test conditions.

Group	No.	Disc 1 vs Disc 2 Rq (μm)	Disc 1 vs Disc 2 speed (rpm)	Lubricant	Lambda (λ)	SRR (%)	Duration (Mc)	Voltage (V)
Macropitting	M1	0.03 vs 0.04	600 vs 631	PAO8	1.15	−10	6	0
	M2	0.03 vs 0.26			0.23		1.5	
	M3						6	
Micropitting	MP1	0.03 vs 0.04	600 vs 631	PAO8 + ZDDP	1.15	−10	6	0
	MP2	0.03 vs 0.26			0.23		1.5	
	MP3						6	
Electrical pitting	E1	0.03 vs 0.04	600 vs 631	PAO8 + ZDDP	1.15	−10	1.5	10
	E2		1200 vs 1262		1.84			
	E3		1200 vs 1395	PAO8	1.91	−20	0.5	

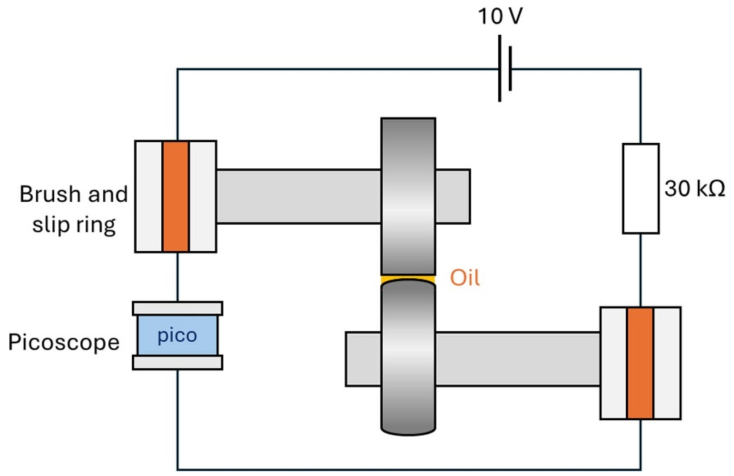

Figure 3. Voltage supply for the disc contact.

dielectric strengths for PAO8 (14–15 kV mm^{-1}) [39, 40], the theoretical breakdown voltage at the minimum oil thickness is estimated to be between 1 and 1.5 V. Interestingly during testing, it was observed that the voltage measurements between the discs never exceeded ~1.4 V. Previous studies have likewise reported that small voltages are sufficient to produce electrical breakdown in lubricated contacts [41].

2.3. Surface topography measurement methods

Post-test analysis involved measurements of surface roughness and topography of the discs. 2D surface profiles and roughness were measured using an Intra Touch profilometer (Taylor Hobson, Leicester, UK), with a vertical range of 1 mm and a resolution of 4 nm. 2D roughness parameters were analysed in this work rather than 3D roughness parameters because portions of the disc surfaces were too smooth to be measured using an optical profilometer due to excessive surface reflection [17]. For each disc, four measurements were taken at angular intervals of 90°. Prior to roughness evaluation, the profiles were levelled and surface form was removed. The profiles were then filtered using a Gaussian filter with cut-off wavelengths selected according to the measured surface characteristics. The filtered surfaces were then analysed using amplitude and functional parameters. Three amplitude parameters defined in ISO 4287, R_q (RMS deviation), R_p (peak), R_v (valley), R_{sk} (skewness), and R_{ku} (kurtosis), were considered. These parameters provide statistical measures of surface height distribution, capturing the overall roughness magnitude (R_q), largest profile peak height (R_p), largest profile valley depth (R_v), distribution asymmetry (R_{sk}), and profile sharpness (R_{ku}) [16].

Furthermore, functional parameters R_k (core roughness depth), R_{pk} (reduced peak height), and R_{vk} (reduced valley depth), as defined in ISO 13565-2, were evaluated. These parameters are derived from the Abbott–Firestone (material ratio) curve [42], as shown in figure 4. The material ratios M_{r1} and M_{r2} define the transitions between the peak, core, and valley regions. A linear regression is fitted to the region of minimum slope, representing the core roughness. The parameter R_k is defined as the vertical distance between the intersections of the extended regression line with the 0% and 100% material ratio levels. The parameters R_{pk} and R_{vk} are determined from the areas between the material ratio curve and the regression

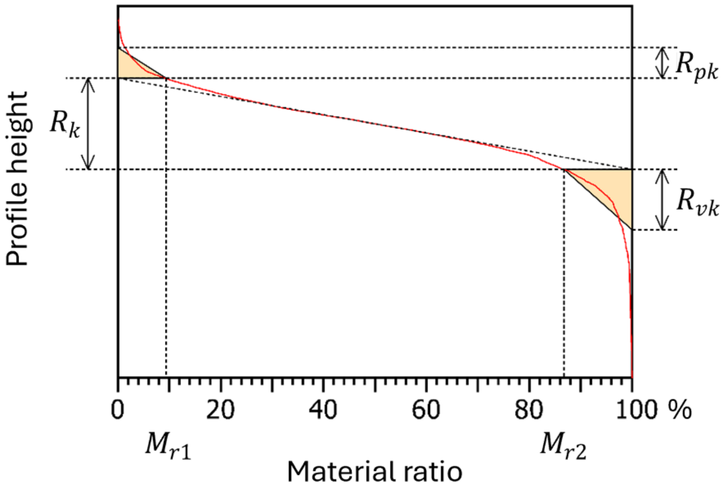

Figure 4. Abbott-firestone (material ratio) curve of a fresh disc surface, shown for indication of functional parameters *Rk*, *Rvk*, and *Rpk*.

line above M_{r1} and below M_{r2}, respectively, and are expressed as the heights of equivalent triangular areas [43].

Additionally, 3D surface measurements were performed using an Alicona G4 profilometer (Alicona Imaging GmbH, Raaba, Austria) with vertical and lateral resolutions of 50 nm and 2 μm, respectively. In the software, the original disc form was removed and the coordinate axes were adjusted to align the unworn surface as the reference plane. Pit depth was determined directly from the 3D topography by measuring the vertical distance from this reference plane to the lowest point of each pit, while pit width was defined as the maximum lateral dimension of the pit at the surface level. To quantify the pitting area, the images were converted into binary format through manual segmentation in ImageJ to identify and separate the pitted regions from the surrounding surface. To observed detailed features, such as crack propagation, the discs were observed using a JEOL JSM-7200F scanning electron microscope (SEM) (JEOL Ltd, Tokyo, Japan).

3. Results

3.1. Optical observations and quantitative pit geometry

Optical images of the 'Macropitting' wear tracks are presented in figure 5. Compared with the untested discs shown in figure 2, the smooth–smooth surface combination (M1 = 1.15) showed only minor wear in the rolling–sliding direction on both discs, with no clear evidence of pitting. As this was the baseline test, the absence of pitting was expected. Decreasing the lambda ratio to 0.23 resulted in small surface cracks initiated on Disc 1 by 1.5 million cycles, but no pitting was observed (M2). By 6 million cycles (M3), macropits were observed, which were characterised by large, irregular surface breakouts with jagged boundaries, with lateral dimensions on the order of hundreds of micrometres.

Optical images of the 'Micropitting' wear tracks are presented in figure 6. Similar to M1, the smooth–smooth test condition (MP1, $\lambda = 1.15$) resulted in only minor wear and no pronounced pitting features, as expected. The difference in M1 and MP1 was the blue tint on the wear track commonly seen in tribological tests with ZDDP containing lubricants, which was identified as ZDDP tribofilm [36]. Under the smooth–rough combination (MP2 and MP3, $\lambda = 0.23$), pits were observed on Disc 1 at 1.5 million cycles (MP2) with features typical of micropitting, characterised by small pits which were tens of micrometres in width with surface confined shapes. After 6 million cycles (MP3), the micropitted regions exhibited slight growth in pit size and area.

It was observed that both macropitting and micropitting occurred exclusively on the smooth discs (Disc 1) in the smooth–rough contact configurations. This behaviour has been explained by the stress transfer mechanism described in [36], where under boundary or mixed lubrication conditions, the stress history is dominated by the rough surface. When a rough surface slides or rolls against a smooth counter surface, the smooth surface is subjected to pronounced pressure fluctuations imposed by the rough surface. Individual asperities on the rough surface form highly localised contacts generating elevated near-surface stresses. These promote crack initiation close to the surface, ultimately leading to the development of pitting.

Optical images of the 'Electrical pitting' wear tracks are presented in figure 7. Unlike the pure RCF test, pits were found on both discs in E1 ($\lambda = 1.15$). The wear tracks were characterised by small and

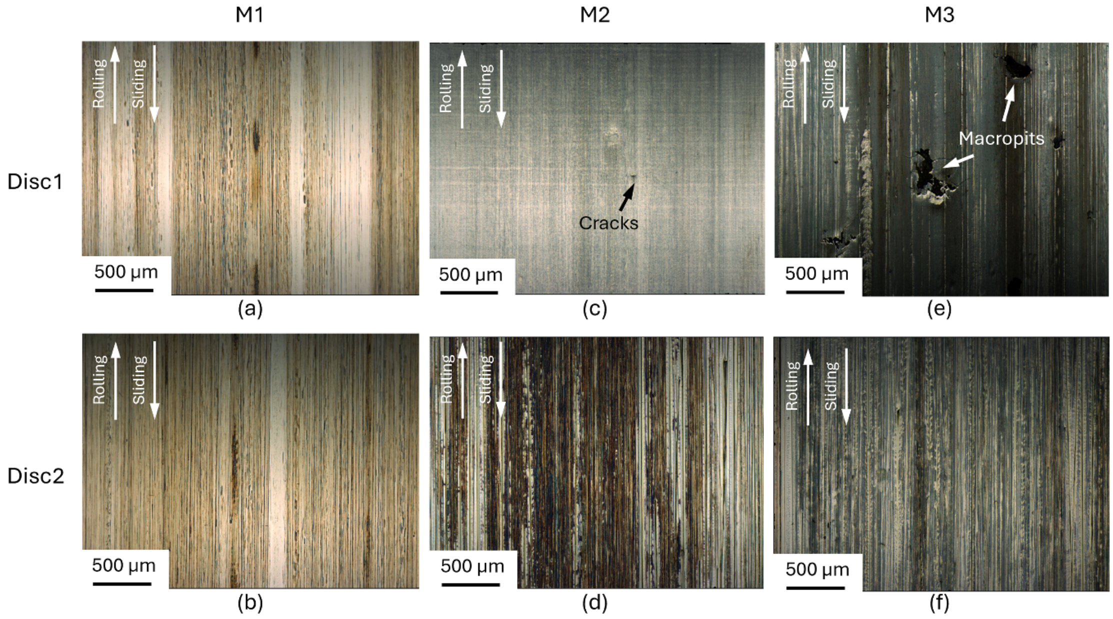

Figure 5. Optical images of wear tracks after macropitting tests.

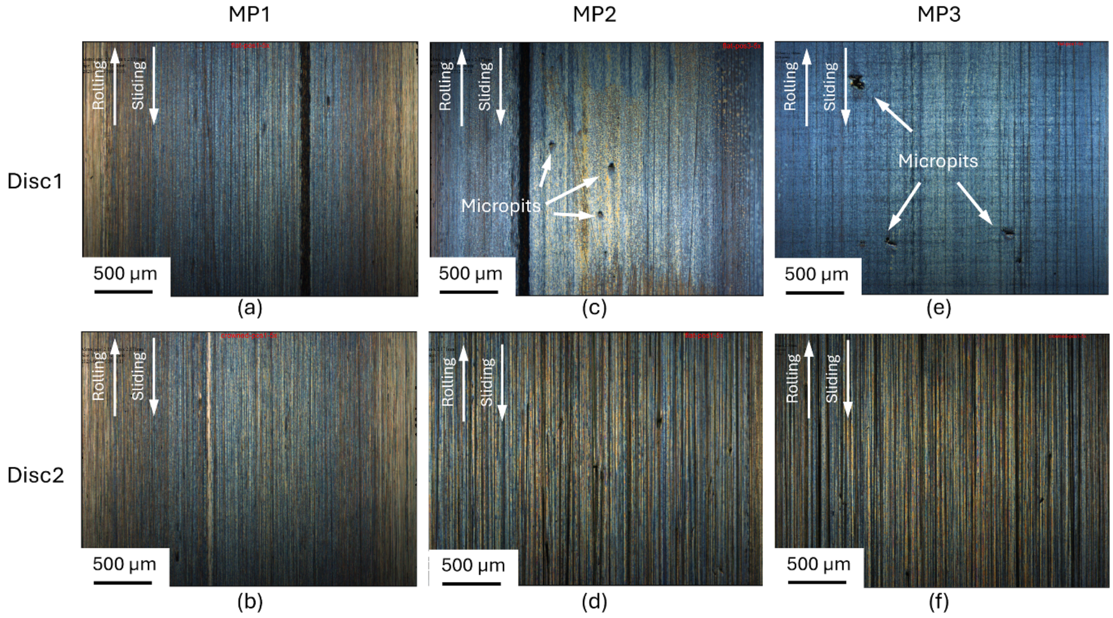

Figure 6. Optical images of wear tracks after micropitting tests.

crater-like pits that tended to occur in localised clusters. With different combinations of lubricant, lambda ratio, and SRR, electrical pits were also found in E2 and E3, supporting the repeatability of producing electrical pitting under the applied-voltage configuration.

To characterise the differences in topography and depth variation among the three pitting modes, 3D optical topography and corresponding height maps were obtained. Representative examples are shown in figure 8 as a qualitative visual representation, while in figure 9 quantitative pit geometry and coverage is explored. For the RCF pitting, mature pit formation was observed in the longest tests (M3 and MP3) and thus characterisation of those tests gives better representation for comparing.

For M3, the macropits had an average width of 475 μm, an average depth of 35 μm, an average volume of 2.2×10^5 μm^3 with a surface coverage of 1.9%. In contrast, for MP3 the micropits had a smaller average width of 138 μm, a shallower depth of 4.9 μm, a smaller volume of 4000 μm^3 with a lower coverage of 0.24%. All the electrical pitting tests were run shorter duration and their pit width (average 32 μm), volume (average 2600 μm^3), and coverage (0.03%–0.15%) were smaller. However, the

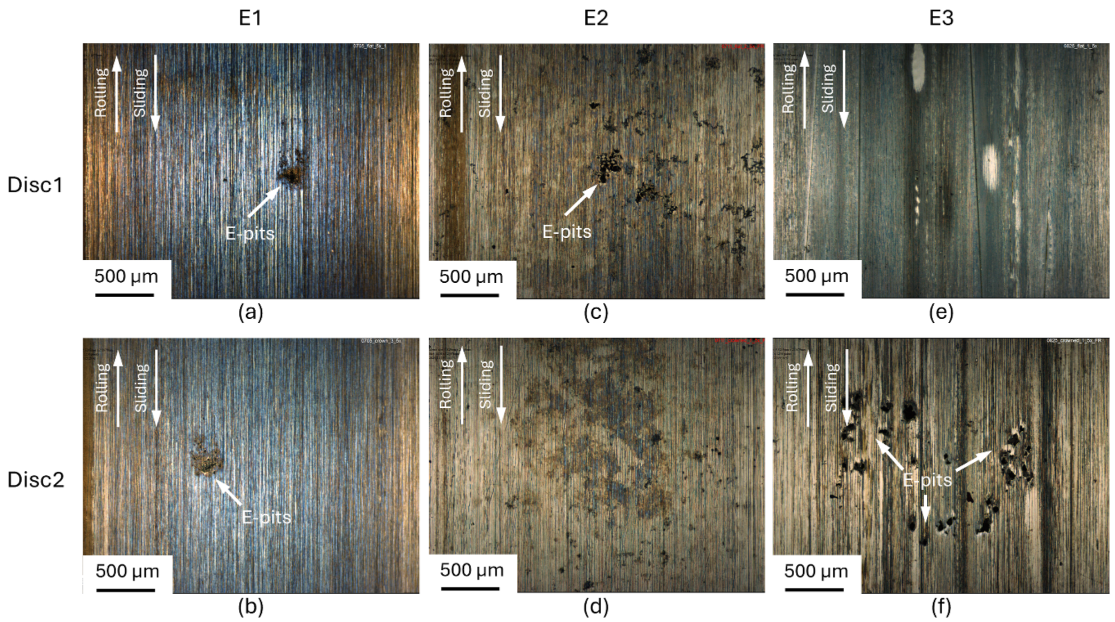

Figure 7. Optical images of wear tracks after electrical pitting tests.

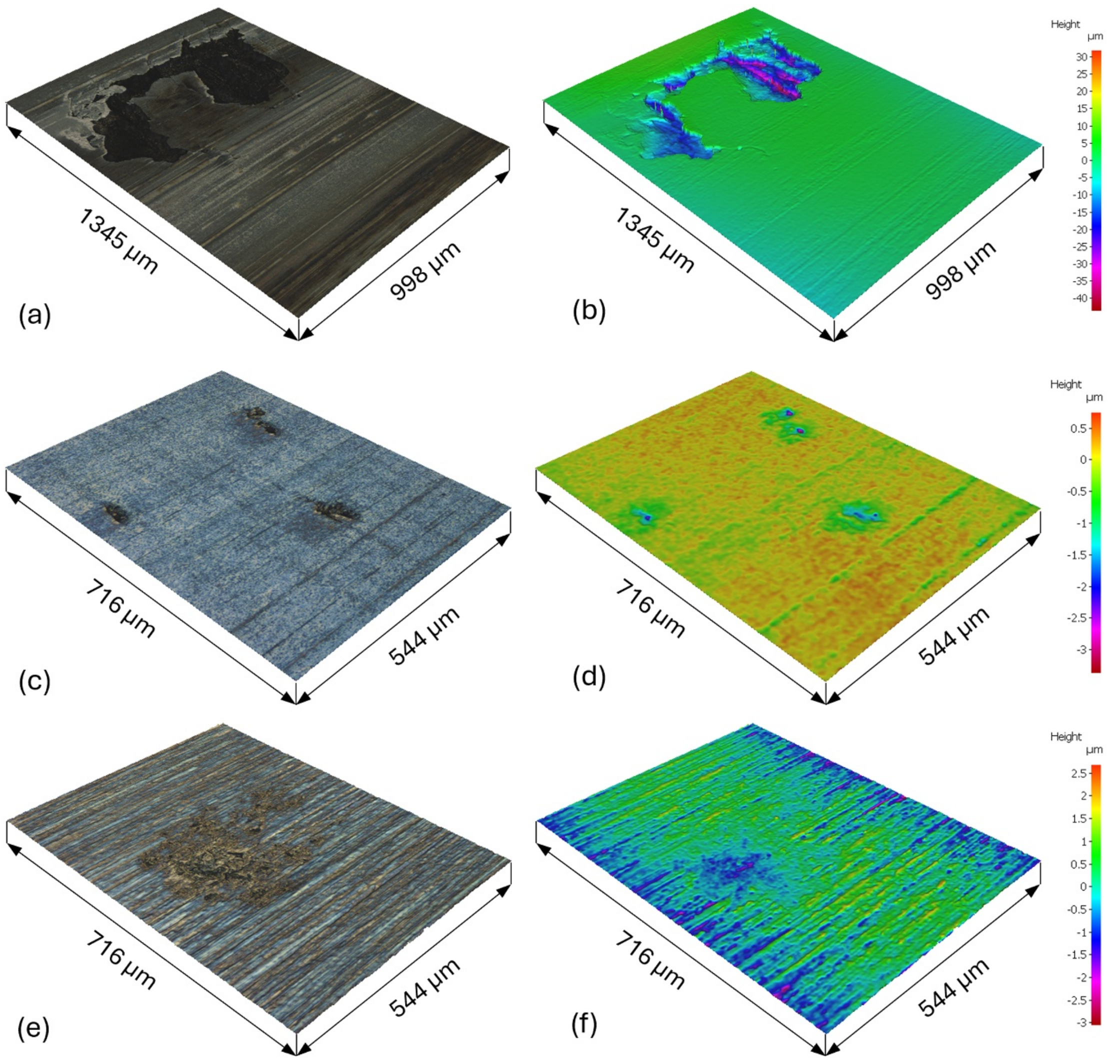

Figure 8. Representative optical images and corresponding height maps of (a), (b) macropitting, (c), (d) micropitting, and (e), (f) electrical pitting.

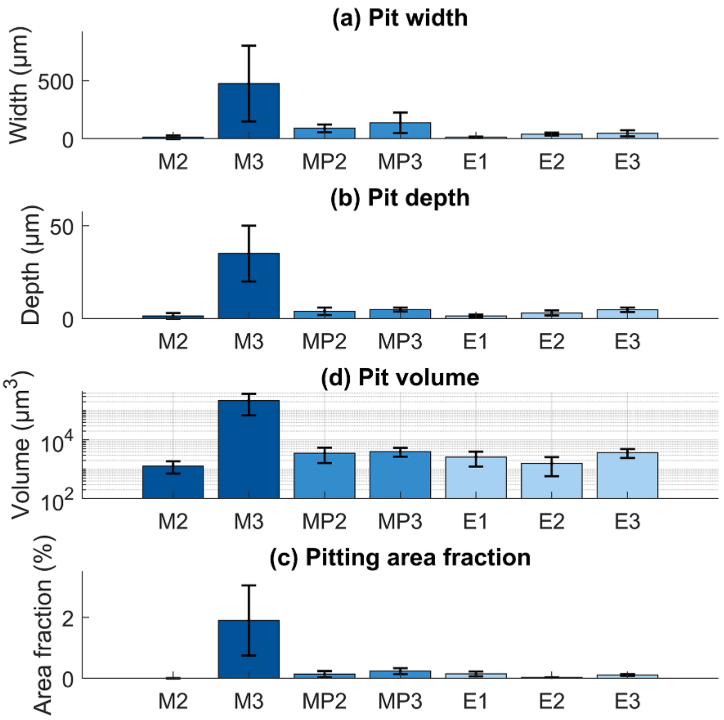

Figure 9. Pit geometry: (a) pit width, (b) pit depth, (c) pitting volume, and (d) pit area fraction for macropitting, micropitting, and electrical pitting tests (mean ± SD).

maximum pit depths reached up to 4.8 μm, comparable to those observed for micropitting.

3.2. SEM observations and mechanism analysis of pitting

SEM was employed to study the pit morphologies at high resolutions. Figure 10 presents images of macropits from Test M3. The pit is characterised by extensive cracks creating regions of fine flakes/plates. The overall morphology is similar to macropits reported in [12, 44]. In the current study, it is further found macropits originated from surface cracks oriented in the axial direction (i.e. transverse to the rolling/sliding direction), from which the pit floor slopes downward against the sliding direction. From the initiation crack, multiple secondary cracks, which can be two to three times longer than the initiation crack, propagated opposite to the sliding direction in a fan-shaped pattern, forming a pitted area with an opening angle of 110–120°, as illustrated by the dotted arrow lines in figure 10. Material detachments subsequently occurred between adjacent cracks due to secondary crack propagation and interaction, leading to an irregular trailing edge with extensive cracking. The secondary crack network and material detachments between adjacent cracks are clearly visible in a pre-mature macropit, as shown in figure 10(a). With continued crack growth and coalescence, material detachments can join, forming large pitted areas on the order of several hundred micrometres, as presented in figures 10(b) and (c).

The occurrence of cracks and pits can be explained by the numerical modelling of the EHL of rough surface contacts presented in [45, 46]. Under low lambda ratios, the frequency and severity of asperity contacts increase, and aggressive asperity interactions can generate highly localised pressure spikes that exceed the nominal maximum Hertzian contact pressure by several orders, increasing the likelihood of crack initiation and subsequent pit formation. However, as this occurred only over several million cycles, it is likely that work hardening led to embrittlement of the material which also contributed.

Figure 11 shows representative micropits from MP3. These crescent-shaped pits are typical of micropitting features reported in the literature [30, 47–49]. The pits originated from surface cracks initiated in the axial direction, as shown in figure 11(a), or at an angle of up to 40° to the axial direction, as shown in figures 11(b) and (c). The geometry of the initiation cracks is approximately outlined by the dotted curves. Subsequently, multiple short secondary cracks developed from the initiation crack and propagated predominantly opposite to the sliding direction. Material detachment between adjacent cracks, as evidenced in figure 11(a), led to the formation of pitted regions.

The initiation cracks, with typical axial lengths of 100–200 μm, largely governed the width of the pits. In contrast, secondary cracks extended only 60–70 μm in the rolling/sliding direction. The confined crack propagation and the shorter length of secondary cracks relative to the initiation cracks resulted in

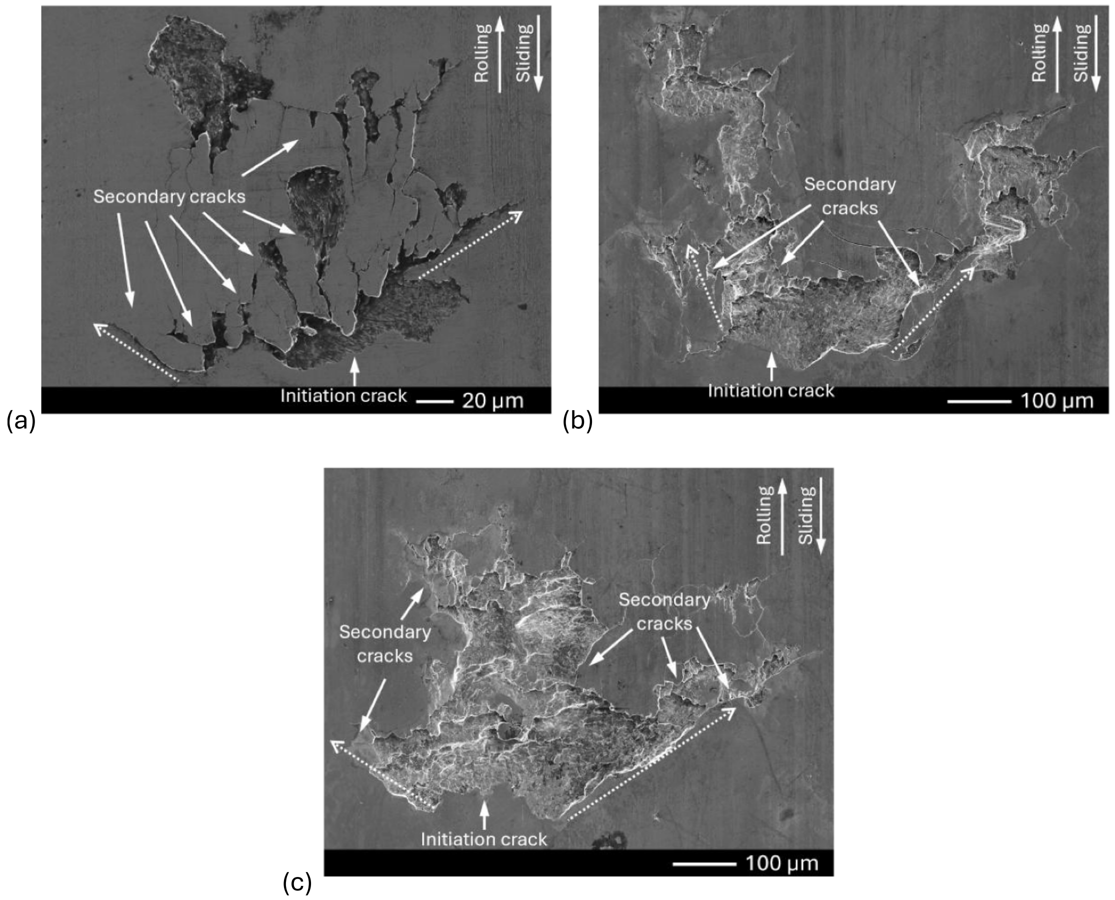

Figure 10. SEM images of macropits after test M3.

the surface-confined crescent-shaped morphology of micropits.

SEM images of electrical pits are shown in figure 12. The crater-like pits exhibited close to circular morphologies with sharp edges, with a circularity of approximately 0.7. These are characteristic features of electrically induced discharge damage reported in previous studies [8, 15]. The pits typically had areas in the range of 310–1200 μm^2, while some larger pits exceeded 2000 μm^2. In test E1, the pits showed more pronounced irregularity, which can be attributed to more severe asperity contact at the lower lambda ratio. The lambda ratios for E1–E3 were 1.15, 1.84, and 1.91, respectively. Apart from pits, grooves and ridges along the rolling/sliding directions were observed.

3.3. Surface roughness evolution

Roughness parameters were measured within the wear scar in the axial direction, with an evaluation length of 2 mm at four positions for each disc. The measurements were positioned in non-pitted areas, because the presence of pits can introduce deep localised valleys that dominate the height distribution and bias roughness parameters. To minimise edge effects, the measurement lines were positioned at least 1 mm away from pitting edges.

Figure 13 presents the average difference of R_q, R_v, R_p, R_{sk}, and R_{ku} of Disc 1 in the pitting tests relative to the untested Disc 1, which had an R_q of 0.03 μm, an R_v of 0.06 μm, an R_p of 0.05 μm, a slightly negative skewness of -0.21 and a nominal kurtosis value of 3.28. Functional roughness parameters are shown in figure 14. The untested surface showed values of $R_k = 0.06$ μm, $R_{vk} = 0.04$ μm and $R_{pk} = 0.03$ μm.

Minimal changes in roughness were observed for the baseline macropitting test, where only minor wear was observed. For the short macropitting test (M2), R_q increased by 25 nm (83%), and R_v and R_p increased by 76 nm (127%) and 53 nm (106%), respectively. The functional parameters showed increases of 127% for R_k and 166% for R_{vk}. The most pronounced surface evolution was observed for the longer macropitting test (M3). R_q increased significantly by 130 nm (433%) and the deepest valley (R_v) increased by 490 nm (817%). Correspondingly, pronounced increases in functional parameters were observed relative to the virgin surface, with R_k, R_{vk}, and R_{pk} increasing by 250%, 660%, and 60%, respectively. The dominant growth in R_q, R_v, and R_{vk} indicates the surface change was governed by valley formation resulting from plastic deformation induced by cyclic stresses.

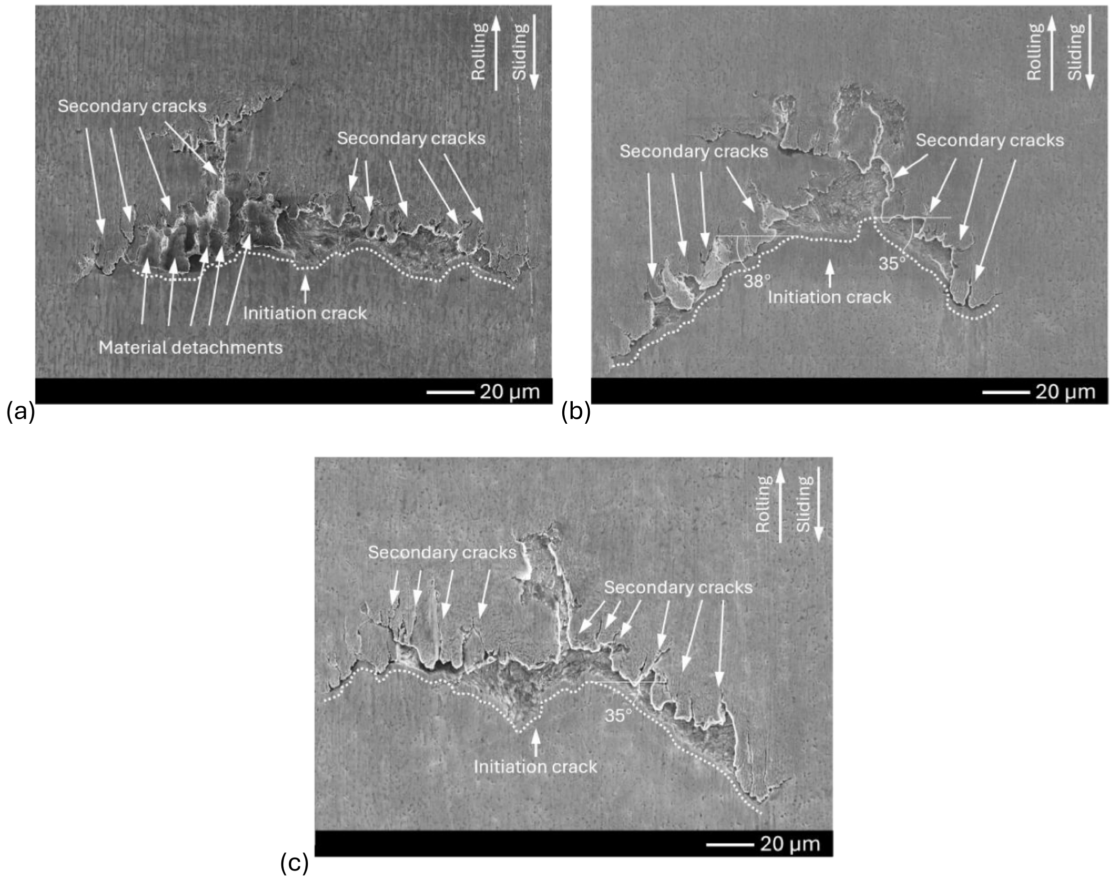

Figure 11. SEM images of micropits after test MP3.

For the micropitting tests, the increases in surface roughness were comparable across all three conditions (MP1, 2, 3), regardless of whether visible micropitting was produced. The magnitude of roughness change was greater than that observed in the baseline macropitting test (M1), but lower than that measured for discs exhibiting surface cracks or macropits (M2 and M3). The increase in R_q ranged from 6 to 20 nm (20%–67%), while R_v increased by 65%–%100 nm (108%–167%) and R_p by 26–50 nm (52%–100%). The functional roughness parameters showed similar trends across the micropitting tests. Compared with the untested surface, R_{pk} remained comparable, whereas R_k and R_{vk} increased by approximately 30%–90% and 70%–88%, respectively. Compared with the macropitting tests, the milder roughness changes indicate that the ZDDP reduced asperity interaction and suppressed significant surface damage.

For the electrical pitting tests, surface roughness exhibited larger increases than those observed in the short macropitting test and all micropitting tests. The increase in R_q ranged from 32 to 61 nm (107%–203%), while R_v increased by 133–181 nm (222%–302%) and R_p by 74–153 nm (148%–306%). Correspondingly, all functional roughness parameters showed significant increases, with R_k increasing by 161%–205%, R_{vk} by 151%–335%, and R_{pk} by 30%–165% relative to the untested surface. The changes are likely due to localised surface melting and resolidification from electrical discharges.

As seen in figure 13(a), increases in R_v were more pronounced than those of R_p. Furthermore, as shown in figure 13(b), a decrease in skewness accompanied by an increase in kurtosis was observed for most of the tests. This indicates that surface evolution in pitting tests was dominated by valley formation, with roughness evolution governed by localised valleys rather than uniform surface modification.

Typical surface profiles are shown in figure 15 to support the roughness analysis, with the shaded yellow regions indicating the wear track. The macropitted surface exhibits pronounced valley features due to material loss, whereas the micropitted surface remains comparatively smooth. The electrically pitted surface shows intermediate behaviour.

Figure 16 presents the average difference of R_q, R_v, R_p, R_{sk}, and R_{ku} of Disc2 relative to the untested Disc2. Specifically, M1, MP1, E1–E3 are compared with the smooth Disc2 (R_q = 0.04 μm), and M2, M3, MP2, and MP3 are compared with the roughened Disc2 (R_q = 0.26 μm). Functional roughness parameters are

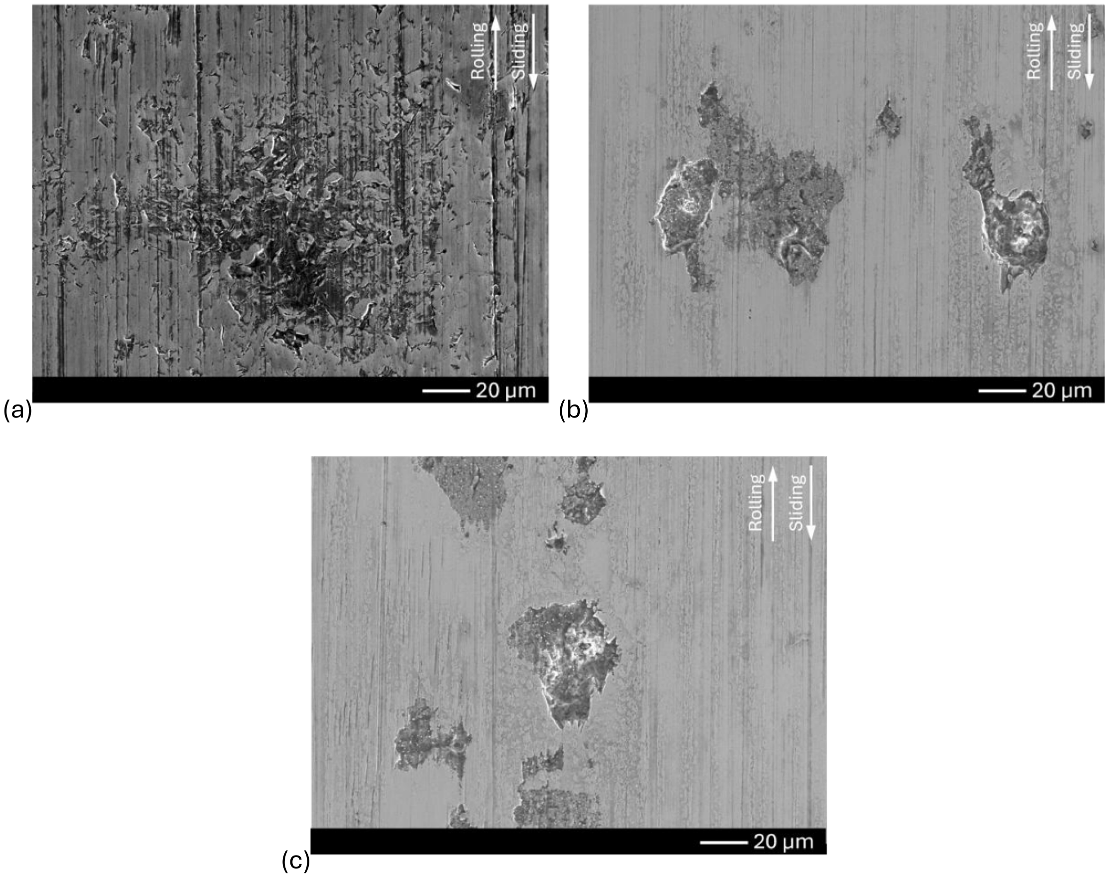

Figure 12. SEM images of electric pits in test (a) E1, (b) E2, and (c) E3.

shown in figure 17. For the smooth discs, only minor to mild changes were observed in the fatigue pitting tests (M1 and MP1), which can be attributed to limited wear under relatively high lambda ratios. Under comparable lambda conditions, the electrical pitting tests resulted in slightly larger changes in roughness due to surface alterations caused by electrical discharge. In contrast, larger changes were observed for the roughed discs in the fatigue pitting tests. In macropitting tests, R_q increased by 67–96 nm (25%–37%) and R_v and R_p increased by 130–200 nm (84%–178%), accompanied by an increase in skewness and a decrease in kurtosis. This suggests the surface became more peak dominated while extreme asperity features were reduced, likely due to plastic deformation during sliding. In micropitting tests, R_q increased by 40–150 nm (15%–58%) and R_v and R_p increased by 156–410 nm (101%–366%), with both skewness and kurtosis increasing. This indicates the development of more pronounced asperities, which may be associated with ZDDP tribofilm formation.

In fatigue pitting tests, the relative changes in Disc 2 were smaller than those for Disc 1. This is consistent with observations in figures 5 and 6, which show that fatigue pitting was predominantly localised on Disc 1, as it was subjected to pronounced pressure fluctuations imposed by the rough Disc 2, as discussed in section 3.1.

4. Discussion

The results demonstrate that macropitting, micropitting, and electrical pitting produce fundamentally different surface topographies that reflect their underlying damage mechanisms. Although all three pitting modes manifest as localised material removal, clear differences were observed in pit size, surface coverage, morphology, crack features, and roughness evolution.

4.1. RCF driven pitting: macropitting and micropitting

Macropitting was characterised by large pits with dimensions on the order of hundreds of micrometres, substantial depths, and extensive surface coverage. In contrast, micropitting produced more than three times smaller, surface-confined pits with limited growth in size and area fraction.

A common feature of both macropitting and micropitting is that pit initiated from surface cracks oriented in the axial direction, followed by material detachments caused by secondary cracks, as observed in figures 10 and 11. Crack initiation and opening are dominated by tensile (Mode I) loading [50, 51]. When tensile stress acts in the rolling/sliding direction, cracks open normal to this stress, resulting in surface crack traces oriented perpendicular to the

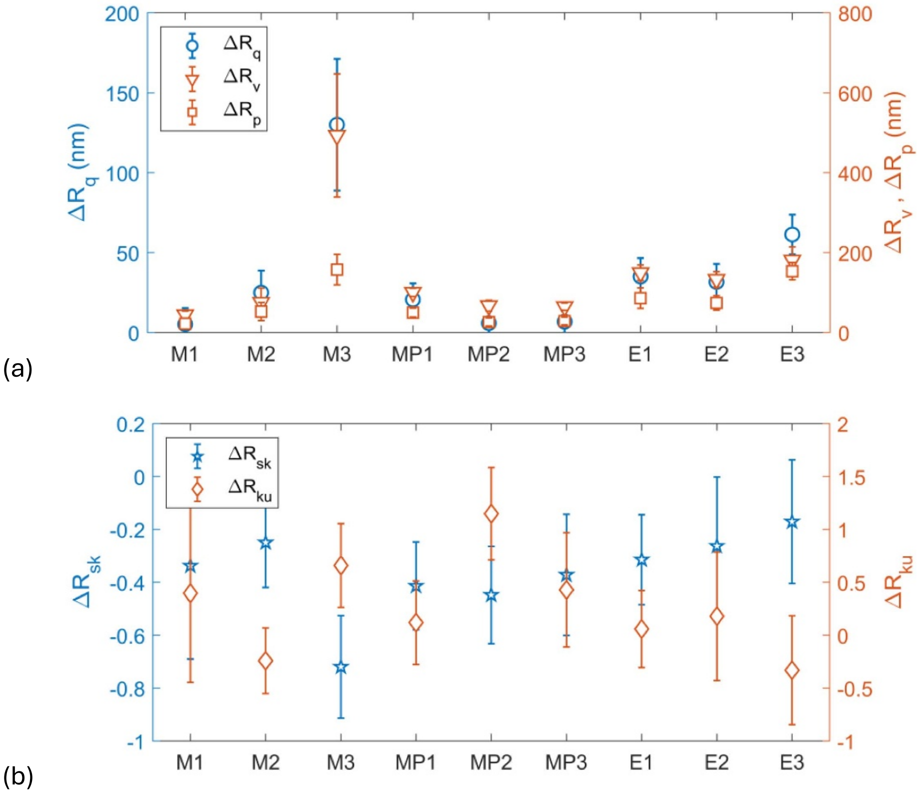

Figure 13. Changes in roughness parameters of Disc 1 surfaces: (a) R_q, R_v, and R_p (b) R_{sk} and R_{ku} for the virgin, macropitted, micropitted, and electrically pitted conditions.

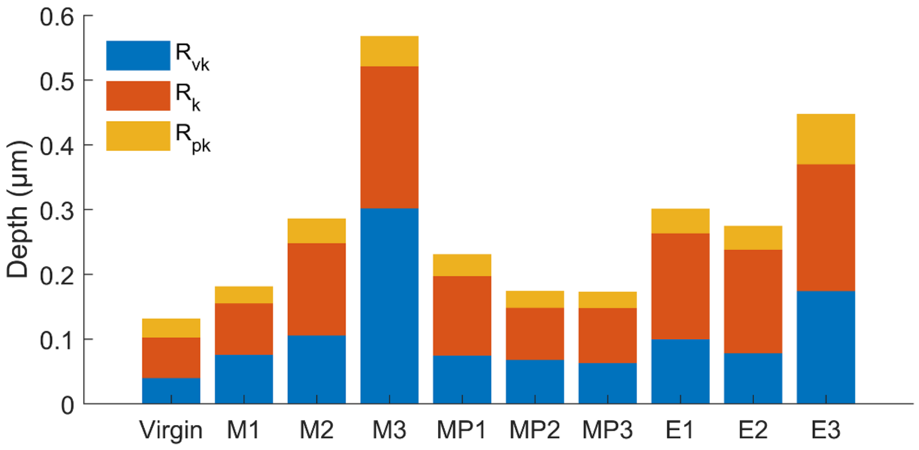

Figure 14. Functional parameters (R_k, R_{pk}, and R_{vk}) of Disc 1 surfaces for the virgin, macropitted, micropitted, and electrically pitted conditions.

rolling/sliding direction, i.e. in the axial direction [47]. As crack growth proceeds, crack paths may deflect, as crack propagation can also be influenced by shear (Mode II) and tearing (Mode III) loading [47].

The difference between macropitting and micropitting is the extent of crack propagation and material liberation. It is observed from figures 5 and 6 that, although macropits initiated later than micropits, their progression was faster. Macropits exhibited aggressive secondary crack growth and coalescence, producing deep and large pits with irregular trailing edges, as illustrated in figure 18(a). In contrast, micropitting produced smaller pits confined to the near-surface region. The initiation crack was relatively short, with multiple shorter secondary cracks propagating from it. Small volumes of material attachments between adjacent cracks resulted in crescent-like shapes, as indicated in figure 18(b).

The difference between macropitting and micropitting can be attributed to the effect of ZDDP, which promotes near-surface crack initiation but only leads to small-scale material liberation and suppressed

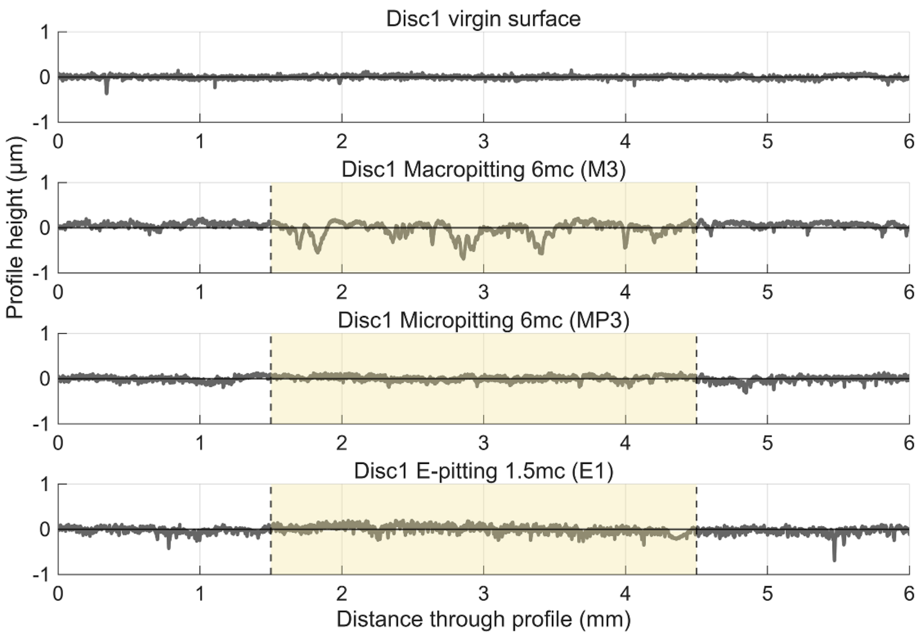

Figure 15. Typical profiles of Disc 1 surfaces for the virgin, macropitted, micropitted, and electrically pitted conditions.

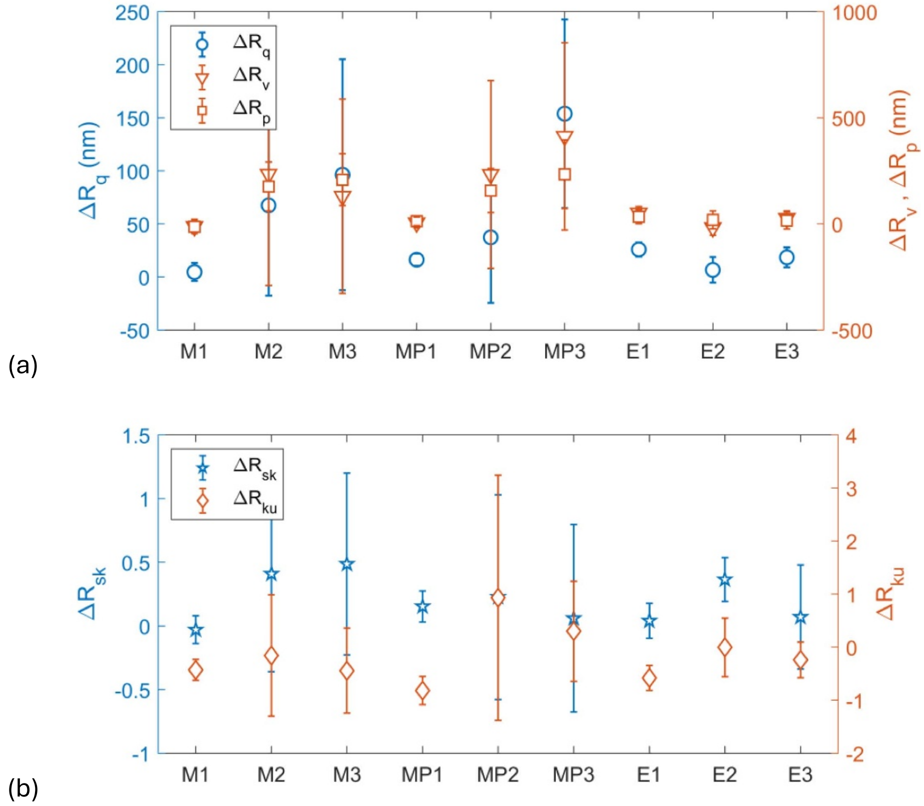

Figure 16. Changes in roughness parameters of Disc 2 surfaces: (a) R_q, R_v, and R_p (b) R_{sk} and R_{ku} for the virgin, macropitted, micropitted, and electrically pitted conditions.

crack propagation. [36, 51] has suggested that elevated surface friction caused by ZDDP tribofilm enhances tensile and shear stresses in the near-surface region, promoting crack initiation. Friction moves the location of the maximum shear stress towards the surface, further increasing the likelihood of surface initiated cracking [51]. Further, ZDDP tribofilm also protects surfaces from wear, enabling accumulation of fatigue and therefore promoting crack initiation. This behaviour is reflected in the roughness and surface profile measurements. In macropitting tests, substantial increases in R_q, R_{sk}, R_k, and R_{vk} were observed,

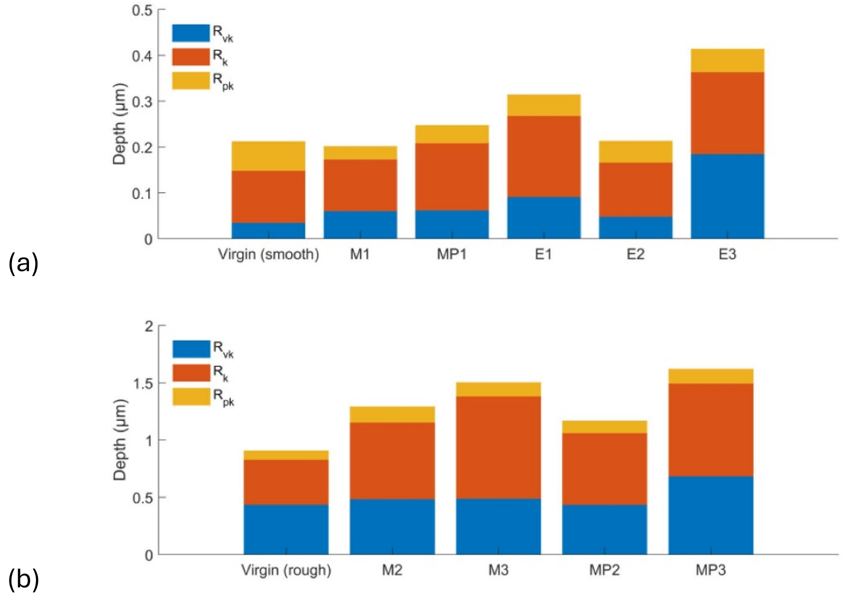

Figure 17. Functional parameters (R_k, R_{pk}, and R_{vk}) of Disc 2 surfaces for the virgin, macropitted, micropitted, and electrically pitted conditions.

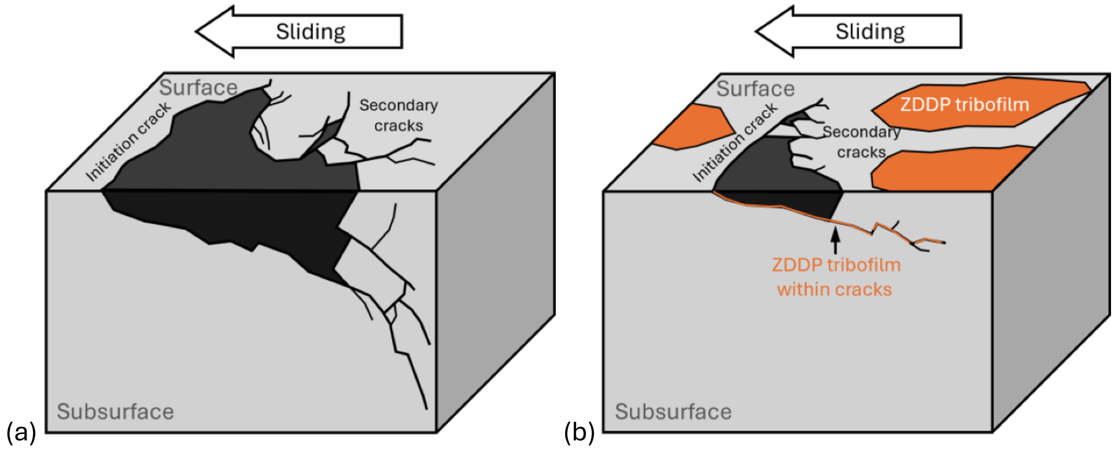

Figure 18. Illustration of formation of (a) macropitting and (b) micropitting.

indicating the formation of deep valleys and severe modification of the load-bearing surface. In contrast, surfaces subjected to micropitting exhibited much smaller changes in roughness parameters, indicating limited material removal. Following initiation, the presence of tribofilm on crack faces increases crack face friction, reducing crack opening and sliding and thereby inhibiting crack propagation and slowing the progression of micropitting.

It has been reported that macropits originated from micropits under prolonged testing durations (6–30 million cycles), high Hertzian contact pressures (>2 GPa), and higher lambda ratios within the mixed lubrication regime, where micropitting severity remained moderate [44]. In the present study, such a transition was not observed, which may be attributed to differences in material properties, test conditions, and test machine configuration. Nevertheless, given the common crack initiation and propagation characteristics identified for both pitting modes, a transition from micropitting to macropitting may occur under extended testing or more severe operating conditions.

4.2. Electrically induced pitting: discharge-dominated material removal

Electrical pitting exhibited a fundamentally different damage signature compared with RCF pitting. Observations revealed crater-like pits with sharp edges, approximately circular morphologies, and a notable absence of surrounding cracks.

Literature indicated in EHL contacts, when the bearing voltage exceeds the dielectric strength of the lubricant film, electrical breakdown occurs and the stored electrical energy is released as an EDM-like pulse through the contact [8, 14]. At microscopic asperity junctions, the resulting high current density causes rapid local melting and vaporisation of the metal; when the discharge ceases, the molten material cools and resolidifies, forming a pit [8, 14].

The circular morphology of the electrical pits has been explained to be due to the axisymmetric nature of the discharge process [52, 53], who employed electro-thermal models with Gaussian-distributed heat flux over a circular plasma channel predicted radially symmetric melting and bowl-shaped craters. In addition, thermo-fluidic modelling showed that subsequent symmetric bubble collapse expelled molten material radially, further reinforcing crater circularity [52].

4.3. Surface roughness and topographical evolution for different pitting modes

Distinct surface roughness and topographical features were observed for the different pitting modes. In [17], surface topography evolution during running-in was investigated using the same bearing steel, test machine, and lubricant viscosity grade. A general reduction in roughness parameters (R_a, R_v, and R_p) was observed under varying entrainment velocity, contact pressure, and slip, indicating surface smoothing as asperity peaks were plastically deformed or mildly worn during running-in. In the present pitting tests, an opposite trend was observed, with increases in surface roughness, particularly in R_q and R_v. This difference reflects a transition from running-in behaviour to damage-dominated surface evolution, where cyclic contact stresses or electrical effects promote roughness growth and valley formation.

Macropitting tests exhibited the largest changes in surface roughness. The pronounced increases in R_q, R_v, and R_{vk} indicate that surface evolution was dominated by valley formation. This behaviour is attributed to cyclic contact stresses that promote near-surface plastic deformation, leading to surface degradation and the development of deep valleys. The resulting increase in surface roughness reduces the lambda ratio, thereby accelerating the progression of macropitting.

In contrast, micropitting tests showed the smallest changes in roughness, which is attributed to the presence of ZDDP tribofilm. The tribofilm, typically 50–150 nm thick [54, 55] and formed preferentially on contact asperities under high shear stress [56], stabilised the surface roughness and mitigated wear by reducing direct metal-to-metal contact [54, 56]. As a result, the tribofilm effectively protected the surface from significant material removal, limiting roughness evolution.

Electrical pitting tests exhibited moderate increases in roughness, exceeding those observed in the short macropitting and all micropitting tests, but remaining lower than those of the long-duration macropitting test. This indicates that the application of an electrical potential altered the surface through repeated discharge events, with evidence of groove-like features along the rolling/sliding direction observed in figure 12.

This work has linked pitting morphology to underlying damage mechanisms using surface topography. While previous studies have examined individual pitting modes in isolation, the present work provides a unified framework that distinguishes fatigue-driven and electrically induced pitting based on pit geometry, crack features, and roughness evolution under controlled rolling–sliding conditions. This mechanistic interpretation enables more reliable diagnosis of pitting origin in practical applications.

5. Conclusions

This study systematically investigated macropitting, micropitting, and electrical pitting in rolling–sliding contacts using a controlled twin-disc tribometer and consistent surface characterisations. The three pitting modes exhibit fundamentally different surface morphologies and damage severities. The main conclusions can be summarised as follows:

1. Macropitting, micropitting, and electrical pitting exhibited distinct morphological characteristics. Macropitting produced large, irregular pits with extensive cracking, with an average pit width of approximately 475 μm. Micropitting generated smaller, confined pits with an average width of 138 μm and a crescent-like morphology. Electrical pitting produced approximately circular pits with an average width of 32 μm, typically occurring in clusters.
2. Both macropitting and micropitting were initiated from surface cracks oriented in the axial direction, indicating a common crack initiation mechanism governed by tensile stresses. However, the extent of secondary crack propagation and material liberation differed substantially. Macropitting was characterised by aggressive secondary crack growth and coalescence, leading to rapid pit growth, while micropitting remained confined due to limited crack propagation.
3. Electrical pitting displayed a fundamentally different formation mechanism from RCF pitting. It is dominated by localised discharge-induced melting and resolidification rather than crack growth. Electrical pitting could occur earlier than fatigue-driven pitting under comparable test durations and resulted in more pronounced surface roughening of the disc surfaces.
4. Roughness measurements revealed clear, mechanism-dependent surface modifications. Macropitting tests exhibited substantial roughness increases, with R_q increasing by up to 130 nm. In

contrast, micropitting tests showed only limited roughness growth (R_q increases of up to 20 nm), reflecting the protective effect of the ZDDP tribofilm in mitigating material removal. Electrical pitting resulted in moderate roughness increases (R_q increases of 32–61 nm), associated with widespread groove formation induced by electrical discharge.

The identified trends in roughness parameters provide insight into the evolution of different pitting modes. While direct topographic measurement is not feasible in practical machinery during operation, the characteristic surface features can serve as failure indicators. They may assist in correlating condition monitoring signals with underlying surface damage mechanisms, thereby supporting failure mode identification in engineering applications.

Acknowledgments

The authors would like to thank the Engineering and Physical Sciences Research Council (EPSRC) funding: EP/S005463/1 Early detection of contact distress for enhanced performance monitoring and predictive inspection of machines for providing financial support for this work. The authors also thank Schaeffler Technologies GmbH &Co. KG for providing the experimental samples.

Data availability statement

The data cannot be made publicly available upon publication because they contain commercially sensitive information. The data that support the findings of this study are available upon reasonable request from the authors.

Author contributions

Zaihao Tian 0000-0002-9612-2410
Data curation (lead), Formal analysis (lead), Investigation (equal), Methodology (equal), Validation (equal), Visualization (lead), Writing – original draft (lead)

Terence Harvey
Formal analysis (equal), Supervision (equal), Writing – review & editing (equal)

Shifeng Zhuo
Data curation (equal), Formal analysis (equal), Methodology (equal)

Haidong Pan
Data curation (equal), Investigation (equal), Methodology (equal)

Robert Wood 0000-0003-0681-9239
Conceptualization (lead), Funding acquisition (lead), Project administration (lead), Resources (lead), Supervision (lead), Writing – review & editing (equal)

References

[1] Liu H, Liu H, Zhu C and Zhou Y 2019 A review on micropitting studies of steel gears *Coatings* **9** 42

[2] Schneider V, Behrendt C, Höltje P, Cornel D, Becker-Dombrowsky F M, Puchtler S, Gutiérrez Guzmán F, Ponick B, Jacobs G and Kirchner E 2022 Electrical bearing damage, a problem in the nano-and macro-range *Lubricants* **10** 194

[3] Peng H, Zhang H, Shangguan L and Fan Y 2022 Review of tribological failure analysis and lubrication technology research of wind power bearings *Polymers* **14** 3041

[4] Ma J, Xue Y, Han Q, Li X and Yu C 2022 Motor bearing damage induced by bearing current: a review *Machines* **10** 1167

[5] Jantara V L Jr and Papaelias M 2020 Wind turbine gearboxes: failures, surface treatments and condition monitoring *Non-Destructive Testing and Condition Monitoring Techniques for Renewable Energy Industrial Assets* (Elsevier) pp 69–90

[6] Aikin A R 2020 Bearing and gearbox failures: challenge to wind turbines *Tribol. Lubr. Technol.* **76** 38–44

[7] Guo L *et al* 2023 *Study on the Electric Discharge Behaviour of a Single Contact in EV Motor Bearings* vol 187 (Tribology International) p 108743

[8] Li Z, Cai R and Nie X 2025 Experimental study: bearing degradation caused by electrical currents and voltages at low speeds *Lubricants* **13** 175

[9] Gloeckner P and Ebert F-J 2010 Micro-sliding in high-speed aircraft engine ball bearings *Tribol. Trans.* **53** 369–75

[10] Zhou R and Mou W 2017 Characterization and mapping of rolling contact fatigue in rail-axle bearings *Eng. Fail. Anal.* **82** 617–30

[11] Symonds N 2004 *Rolling contact fatigue–review and case study Conf. Proc. NATO-RTA-AVT-109: The Control and Reduction of Wear in Military Platforms. Session*

[12] Errichello R 2012 Morphology of micropitting *Gear Technol.* **4** 74–81

[13] Kissling U 2012 Application of the first international calculation method for micropitting *Gear Technol.* **5** 54–60

[14] He F, Xie G and Luo J 2020 Electrical bearing failures in electric vehicles *Friction* **8** 4–28

[15] Janik J R, Saha S, Jackson R L and Mills G 2024 Exploring the boundaries of electrically induced bearing damage in grease-lubricated rolling contacts *Lubricants* **12** 268

[16] Gadelmawla E, Koura M M, Maksoud T M A, Elewa I M and Soliman H H 2002 Roughness parameters *J. Mater. Process. Technol.* **123** 133–45

[17] Harvey T J *et al* 2025 Changes in surface topography during running-in of bearing steel contacts under mixed lubrication *Surf. Topogr. Metrol. Prop.* **13** 035020

[18] Roy S, White D and Sundararajan S 2018 Correlation between evolution of surface roughness parameters and micropitting of carburized steel under boundary lubrication condition *Surf. Coat. Technol.* **350** 445–52

[19] Prajapati D K and Tiwari M 2020 Experimental analysis of contact fatigue damage using fractal methodologies *Wear* **450** 203262

[20] Prajapati D K and Tiwari M 2020 Experimental investigation on evolution of surface damage and topography parameters during rolling contact fatigue tests *Fatigue Fract. Eng. Mater. Struct.* **43** 355–70

[21] Poletto J C, Fernandes C M C G, Barros L Y, Neis P D, Pondicherry K, Fauconnier D, Seabra J H O, De Baets P and Ferreira N F 2023 Identification of gear wear damage using topography analysis *Wear* **522** 204837

[22] Cardoso N, Martins R C, Seabra J H O, Igartua A, Rodríguez J C and Luther R 2009 Micropitting performance of nitrided steel gears lubricated with mineral and ester oils *Tribol. Int.* **42** 77–87

[23] Martins R, Seabra J and Magalhães L 2008 Austempered ductile iron (ADI) gears: power loss, pitting and micropitting *Wear* **264** 838–49

[24] Tian Z *et al* 2025 *Monitoring and Mapping of Pitting in Bearing Steel Contacts* via *Vibration-Based Analysis* (Tribology International) p 111563

[25] Ai X 2013 *Rolling Element Bearing Surface Finish Encyclopedia of Tribology* (Springer) pp 2927–32

[26] Vrček A *et al* 2019 Micro-pitting damage of bearing steel surfaces under mixed lubrication conditions: effects of roughness, hardness and ZDDP additive *Tribol. Int.* **138** 239–49

[27] Rycerz P and Kadiric A 2019 The influence of slide–roll ratio on the extent of micropitting damage in rolling–sliding contacts pertinent to gear applications *Tribol. Lett.* **67** 1–20

[28] Farfan-Cabrera L, Hernández-Peña A, Resendiz-Calderon C D, Lee P, Sanchez C, Lee S and Erdemir A 2025 Electrified four-ball testing of ZDDP and MoDTC as additives in low-viscosity synthetic oil *Wear* **571** 205835

[29] Ali M K A, Zhang C, Yu Q, Sun Y, Zhou F and Liu W 2025 Do electrification-temperature effects deteriorate ZDDP tribofilms in electric vehicles transmission? Insights into antiwear mechanisms using low-SAPS oils *Wear* **564** 205746

[30] Rycerz P, Olver A and Kadiric A 2017 Propagation of surface initiated rolling contact fatigue cracks in bearing steel *Int. J. Fatigue* **97** 29–38

[31] Zhou Y *et al* 2019 The effect of contact severity on micropitting: simulation and experiments *Tribol. Int.* **138** 463–72

[32] Brizmer V, Matta C, Nedelcu I and Morales-Espejel G E 2017 The influence of tribolayer formation on tribological performance of rolling/sliding contacts *Tribol. Lett.* **65** 57

[33] Esmaeili K, Wang L, Harvey T J, White N M and Holweger W 2023 A study on the influence of electrical discharges on the formation of white etching cracks in oil-lubricated rolling contacts and their detection using electrostatic sensing technique *Lubricants* **11** 164

[34] Arakere N K 2016 Gigacycle rolling contact fatigue of bearing steels: a review *Int. J. Fatigue* **93** 238–49

[35] Wandel S, Bartschat A, Glodowski J, Bader N and Poll G 2023 Wear development in oscillating rolling element bearings *Lubricants* **11** 117

[36] Tian Z *et al* 2024 Influence of ZDDP tribofilm on micropitting formation and progression *Tribol. Int.* **199** 109938

[37] Lokhande R, Mishra S K, Ronanki D, Shakya P, Edachery V and Koottaparambil L 2025 Review on tribological and vibration aspects in mechanical bearings of electric vehicles: effect of bearing current, shaft voltage, and electric discharge material spalling current *Lubricants* **13** 349

[38] Spikes H 2015 Basics of EHL for practical application *Lubr. Sci.* **27** 45–67

[39] Yin Y *et al* 2025 Frequency-dependent molecular relaxation and interfacial polarization in electrical pitting: unveiling tribochemical mechanisms in PAO8 under alternating electric fields *Tribol. Int.* **214** 111296

[40] Jablonka K, Glovnea R and Bongaerts J 2012 Evaluation of EHD films by electrical capacitance *J. Phys. D: Appl. Phys.* **45** 385301

[41] Torres J and Dhariwal R 1999 Electric field breakdown at micrometre separations *Nanotechnology* **10** 102

[42] Salcedo M C, Coral I B and Ochoa G V 2018 Characterization of surface topography with Abbott firestone curve *Contemp. Eng. Sci.* **11** 3397–407

[43] Pawlus P, Reizer R, Wieczorowski M and Krolczyk G 2020 Material ratio curve as information on the state of surface topography—a review *Precis. Eng.* **65** 240–58

[44] Wainwright B and Kadiric A 2025 Surface fatigue in lubricated contacts: mapping the failure modes of micropitting versus macropitting *Int. J. Fatigue* **197** 108908

[45] Evans H P, Snidle R W, Sharif K J and Bryant M J 2012 Predictive modelling of fatigue failure in concentrated lubricated contact *Faraday Discuss.* **156** 105–21

[46] Clarke A, Evans H P and Snidle R 2016 Understanding micropitting in gears *Proc. Inst. Mech. Eng. C* **230** 1276–89

[47] Ren Z, Li B and Zhou Q 2022 Rolling contact fatigue crack propagation on contact surface and subsurface in mixed mode I+ II+ III fracture *Wear* **506** 204459

[48] Soltanahmadi S *et al* 2017 Tribochemical study of micropitting in tribocorrosive lubricated contacts: the influence of water and relative humidity *Tribol. Int.* **107** 184–98

[49] Ueda M, Spikes H and Kadiric A 2019 *In-situ* observations of the effect of the ZDDP tribofilm growth on micropitting *Tribol. Int.* **138** 342–52

[50] Sun C-T and Jin Z 2011 *Fracture Mechanics* (Academic Press)

[51] Ueda M, Wainwright B, Spikes H and Kadiric A 2022 The effect of friction on micropitting *Wear* **488** 204130

[52] Tao J, Ni J and Shih A J 2012 Modeling of the anode crater formation in electrical discharge machining *J. Manuf. Sci. Eng.* **134** 011002

[53] Shao B and Rajurkar K P 2015 Modelling of the crater formation in micro-EDM *Proc. CIRP* **33** 376–81

[54] Zhang J and Spikes H 2016 On the mechanism of ZDDP antiwear film formation *Tribol. Lett.* **63** 1–15

[55] Spikes H 2004 The history and mechanisms of ZDDP *Tribol. Lett.* **17** 469–89

[56] Spikes H 2025 Mechanisms of ZDDP—an update *Tribol. Lett.* **73** 38